Journal of Materials Chemistry A

PAPER

View Article Online
View Journal

Cite this: DOI: 10.1039/c6ta06879k

Mg-doped TiO_2 boosts the efficiency of planar perovskite solar cells to exceed 19%

Huiyin Zhang, Jiangjian Shi, Xin Xu, Lifeng Zhu, Yanhong Luo, Dongmei Li and Qingbo Meng*

Received 11th August 2016
Accepted 31st August 2016

DOI: 10.1039/c6ta06879k

www.rsc.org/MaterialsA

Mg as an effective ion dopant has been introduced into compact TiO_2 ETL for planar perovskite solar cells. It is found that Mg doping can shift the Fermi energy level of the ETL upward and decrease the resistivity of the TiO_2 film. Carrier transport velocity is thus enhanced and high charge collection efficiency has been achieved at high bias voltages, leading to a higher fill factor (FF) and better cell efficiency. More than 19% power conversion efficiency has been obtained.

Introduction

Perovskite solar cells (PSCs), consisting of a perovskite absorber and inorganic or organic selective contacts, have attracted considerable interest as a promising candidate for photovoltaic application.[1–6] Typically, PSCs can be fabricated by solution-processing methods, which have distinctive advantages of low manufacturing cost and simple procedures, compared to the conventional high temperature based inorganic semiconductor junction cells.[1–5] In the past few years, the power conversion efficiency (PCE) of this cell has been enhanced from 3.8% to 22.1%, which is even higher than that of multicrystalline silicon solar cell (21.3%) and comparable to those of CdTe (22.1%) and Cu(In, Ga)Se_2 (22.3%) solar cells.[7] To date, most of the certified high-efficiency cells are based on mesoscopic structures,[8–11] which can provide larger interface contact area to support film deposition and afford faster charge extraction. In fact, the planar heterojunction PSCs have also been developing rapidly, with a series of solution or vapor deposition methods applied to obtain high-quality perovskite film.[12–17] This planar PSC has a simpler device structure and can be completely fabricated at much lower temperature, which help to lower the fabrication cost. Due to these advantages, many works have also been focused on the planar cell.

In addition to a high quality perovskite absorber film,[11–15] engineering selective contact layers and interfaces has also been demonstrated as an effective approach to improve cell performance.[16–21,40–44] In planar PSCs, the n-type electron transport layer (ETL) plays an important role in extracting photo-induced free electrons and suppressing front-surface hole recombination. Therefore, the compact ETLs have to fully cover the conductive substrate.[32] Usually, a TiO_2 ETL with a thickness of tens of nanometers is demanded to satisfy this coverage; however, it simultaneously suffers from low conductivity and carrier accumulation due to the numerous trap states.[33] Thus, it is crucial to enhance the ETL's carrier transport ability while keeping its covering advantage. Therefore, some works have been carried out. For example, TiO_2 nanoparticles were directly applied to deposit the ETL to increase the electron density and conductivity. Remarkably, the conductivity was increased by 50-fold compared with conventional TiO_2 film.[18,33] Graphene and graphene quantum dots were also introduced as additives to increase the conductivity and carriers extraction of ETL.[22,23] Moreover, ion doping is another effective method to control the trap states and carrier transport, for example, niobium and lithium dopants have been successfully applied.[24–27] These results show that ion doping can effectively tailor the energy band structure, increase the conductivity and decrease trap density of ETL. However, ion doped TiO_2 ETLs were achieved by adding corresponding metal salt into the TiO_2 precursor solution. This method may need a complex sol–gel process, which increases the difficulty to control experiment process.

In this study, magnesium as an effective dopant is introduced into the compact TiO_2 ETL and applied for the planar PSCs. It is found that the Mg doping can shift the Fermi energy level of the ETL upward, increase the free electron density and decrease the density of deep trap states. The resistivity of the TiO_2 film is thus decreased, leading to a decrease in the series resistance of the cell. A PCE exceeding 19% has been achieved. Furthermore, the microscopic carrier transport and recombination mechanisms behind the macroscopic efficiency are further investigated by DC current–voltage, AC frequency impedance and modulated transient photocurrent/photovoltage analysis. It is revealed that Mg doping can significantly reduce the transport time of photo-induced carriers to be collected and enhance the charge collection efficiency at high bias voltages, thus contributing to high performance.

Key Laboratory for Renewable Energy, Beijing Key Laboratory for New Energy Materials and Devices, Institute of Physics, Chinese Academy of Sciences, Beijing 100190, P. R. China. E-mail: qbmeng@iphy.ac.cn

Experimental details

Materials

PbI_2 and $PbBr_2$ were purchased from Aldrich-Sigma (99.9985%); methylammonium bromide (MABr) and formamidinium iodide (FAI) were from Shanghai Materwin New Materials Co., Ltd. *N*,*N*-Dimethylformamide (DMF), dimethylsulfoxide (DMSO) and chlorobenzene were from Alfar Aesar. Spiro-OMeTAD was from Luminescence Technology Corp. Magnesium chloride was purchased from Sinopharm Chemical Reagent Co., Ltd. All the chemicals were directly used without further purification. Laser-patterned FTO glass (Pilkington, thickness of 2.2 mm and sheet resistance of 15 Ω sq^{-1}) was sequentially cleaned with a mild detergent, distilled water and ethanol in an ultrasonic bath. The substrate was treated with UV-ozone for 15 min prior to use.

Device fabrication

The perovskite solar cells are fabricated on the transparent FTO substrate. The compact TiO_2 layer of about 30 nm was deposited onto the FTO by spin coating a sol–gel precursor solution containing 0.125 M titanium isopropoxide and 0.125 M HCl in *n*-butylalcohol and sintered at 500 °C for 30 min. After cooling to room temperature, the TiO_2 compact film was immersed into a 0.025 M $TiCl_4$ aqueous solution with different $MgCl_2$ concentration (0, 0.005, 0.01, 0.025 M) and heated at 70 °C for 30 min. Furthermore, the film was sintered at 500 °C for another 30 min. The perovskite layer was deposited on top of the TiO_2 compact layer by a spin coating method, as reported previously. In detail, the perovskite precursor solution was obtained by dissolving 1.15 mM-PbI_2, 1.095 mM-FAI, 0.202 mM-$PbBr_2$ and 0.202 mM-MABr in a mixture of 0.8 mL-DMF and 0.2 mL-DMSO, then stirring overnight. The perovskite film was successively deposited by two-step spin-coating; first, at 1000 rpm for 10 s and then at 5000 rpm for 30 s. During the second step, 120 μL chlorobenzene was poured on the spinning substrate in 15 s. The as prepared perovskite film was treated at 150 °C for 10 min in the glove box and then 100 °C for 40 min in the vacuum condition. The Spiro-MeOTAD layer with a thickness of about 200 nm was spin-coated onto the perovskite film at 3000 rpm for 30 s. An 80 nm-thick Au electrode was finally deposited *via* thermal evaporation under the vacuum of 10^{-7} Torr.

Characterization

The thickness of the TiO_2 film was measured by a surface profiler (KLA-Tencor). The morphology of the films was obtained by scanning electron microscopy (SEM, Hitachi S4800). X-ray photoelectron spectroscopy (XPS) was performed on the Thermo Scientific ESCALab 250Xi using 200 W monochromated Al Kα radiation, and 500 μm X-ray spot was used for XPS analysis with the energy resolution of 50 meV. The ICP-AES results were obtained by using a full spectrum direct reading plasma spectrometer (IRIS Intrepid II XDL, Thermo Elemental). For the current–voltage (*I–V*) measurements, the cells were illuminated under AM 1.5 simulated sunlight (100 mW cm^{-2}) from Zolix SS150A. *I–V* curves were recorded by a digital source meter (Keithley model 2602). The solar cells were masked with a black aperture to define the active area of 0.1 cm^2. External quantum efficiency (EQE) of the cells was measured with a lab-made setup under 0.3–0.9 mW cm^{-2} monochromic light illumination without bias illumination.[34,35] Transient photovoltage and photocurrent of the cell were obtained by a pulsed double-frequency Nd:YAG laser (Brio, 20 Hz, 4 ns) at 532 nm with an ultralow light intensity of about 10 nJ cm^{-2} and recorded by a sub-nanosecond resolved digital oscilloscope (Tektronix DPO 7104) with input impedances of 1 MΩ and 50 Ω. A signal generator (Tektronix AFG 3052C) together with a low-pass filter was applied to give steady-state bias voltages over the cell. Impedance spectra measurements were performed with an IM6ex electrochemical workstation (Zahner) in dark in the frequency range of 1 MHz–1 Hz and perturbation amplitude of 10 mV.

Results and discussion

In this study, the planar-heterojunction perovskite solar cell was fabricated and Fig. 1(a) shows the device structure of FTO/Mg-doped TiO_2/perovskite film/Spiro-MeOTAD/Au. According to the cross sectional SEM image of the complete cell in Fig. 1(b), different layers are deposited closely to each other; however, the ETL is too thin to be observed. To realize trace-Mg doping and to avoid the formation of insulating MgO secondary phase, Mg doping is accomplished in the $TiCl_4$ treatment process. Herein, the strong acidity of $TiCl_4$ aqueous solution prevents the direct precipitation of MgO. The Mg ions may be embed into the TiO_2 lattice by absorbing into the hydrated TiO_2 and ion diffusion occurs in the later high-temperature sintering process. To confirm the existence of Mg in the ETL layer, ICP-AES measurement is performed, as shown in Fig. 1(c). It clearly shows an emission peak corresponding to Mg atom at about 279 nm and further indicates that the atom ratio between Mg and Ti is about 0.8%. XPS spectra of the ETL films are also measured and shown in Fig. 1(d). The Mg 1s peak is observed and magnified in the inset. To investigate the influence of the existence of Mg atoms in the film, the high-resolution Ti 2p peaks are shown in Fig. 1(e). With Mg, the Ti $2p_{3/2}$ peak is shifted toward the high energy by about 70 meV, which implies that trace Mg has been located into the TiO_2 lattice, influencing the electronic structure of the Ti atoms. Thus, Mg can be considered as a dopant in TiO_2. For clarity, the Mg-doped ETL film will be labeled as 'Mg doped TiO_2 (*x*)' in the following discussion, where '*x*' is the concentration of $MgCl_2$ added in the $TiCl_4$ solution. The XPS valence band spectra are given to further reveal the influence of Mg doping on the electronic structure, as in Fig. 1(f). It is found that the Fermi energy level of the ETL is upward-shifted by about 100 meV, which is obviously larger than the energy resolution of the XPS measurement. However, no change is found in the absorption spectra, suggesting that the band gap of the film has not been changed. Thus, it is deduced that the upward shift of Fermi energy level implies that the free electron density in the film is significantly increased or that the density of deep trap states below the conduction band is decreased.[31] Obviously, these two effects can enhance the charge transport ability of the ETL film.

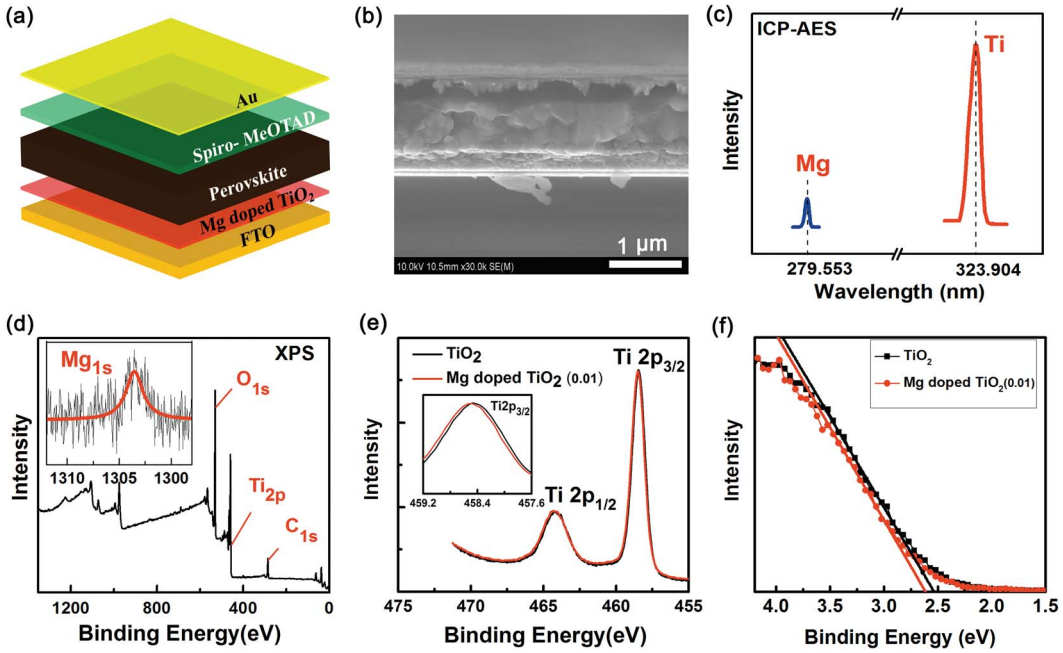

Fig. 1 (a) Schematic and (b) cross sectional SEM image of the planar cell. (c) ICP-AES result of the ETL film on the SiO_2 substrate. (d) XPS full spectrum of the Mg-doped TiO_2 ETL film and the inset is the peak of Mg 1s. (e) Ti 2p peak and (f) valence band spectra of the ETL films with and without the Mg doping.

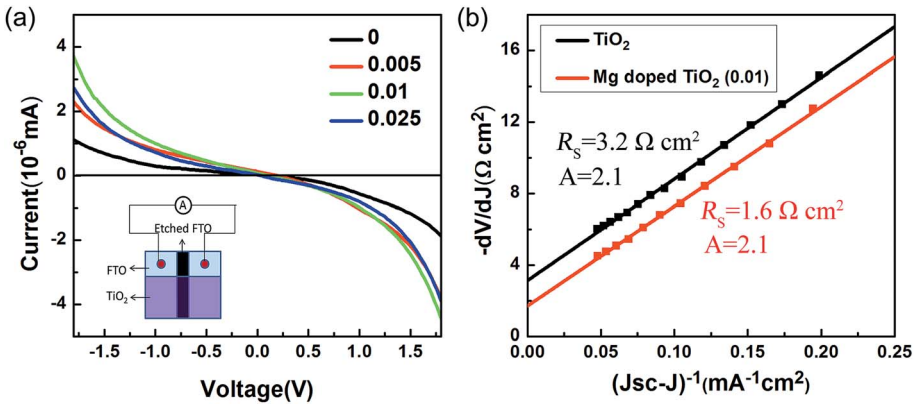

Fig. 2 (a) Conductivity measurement results of the films with different concentration of Mg treatment. The inset depicts the sample structure for this measurement. (b) Plots of dV/dJ *vs.* $(J_{SC} - J)^{-1}$ derived from the illuminated I–V curves (Fig. 3(a)) and the linear fitting curves to obtain the series resistance (R_S) and ideality factor (A) of the cells.

Furthermore, the conductivity of the ETL films is directly measured with a DC I–V method.[24] The sample structure for this measurement is depicted as in the inset of Fig. 2(a). It is obvious that the resistivity of the film is reduced after Mg doping. Among these samples, the ETL doped with 0.01 M Mg shows the highest conductivity, which is about 1.7 times higher than that of the pristine TiO_2 ETL. The series resistance (R_S) of the cells fabricated with and without the Mg-doped ETL is also derived from the illuminated I–V curves,[28] as shown in Fig. 2(b). Agreeing with the resistivity measurement, R_S of the cell is decreased from 3.2 to 1.6 Ω cm^2. In a solar cell, a lower R_S is necessary to eliminate charge loss at high bias voltages and to achieve high fill factor (FF).[24,28] With these ETLs, the cells are fabricated. The statistic results of their performance are summarized in Table 1. As can be observed, Mg doping mainly improves the FF by about 4.3% and slightly increases the open-circuit voltage (V_{OC}) by about 2.8%. Finally, the averaged PCE is enhanced from 16.37% to 17.65% and the highest PCE is improved from 17.29% to 19.08% when 0.01 M $MgCl_2$ is applied as the doping source. For clarity, the I–V curves of the best performed cells with and without the Mg doped ETL and the statistic histograms of the PCE are shown in Fig. 3. As has been discussed, the I–V curves indicate the decrease in R_S. Moreover, these I–V results also indicate that the heterojunction nature of

Table 1 Statistic results of the cell performance with different ETLs

ETL	Averaged J_{SC} (mA cm^{-2})	Averaged V_{OC} (V)	Averaged FF (%)	PCE (%)	
				Average	Max
TiO_2	21.36 ± 0.64	1.060 ± 0.014	72.3 ± 2.4	16.37 ± 0.72	17.29
Mg doped TiO_2 (0.005)	21.46 ± 0.81	1.073 ± 0.017	73.4 ± 1.7	16.89 ± 0.71	17.75
Mg doped TiO_2 (0.01)	21.48 ± 0.60	1.090 ± 0.012	75.4 ± 1.8	17.65 ± 0.75	19.08
Mg doped TiO_2 (0.025)	21.22 ± 0.58	1.080 ± 0.013	74.6 ± 1.8	17.10 ± 0.79	18.24

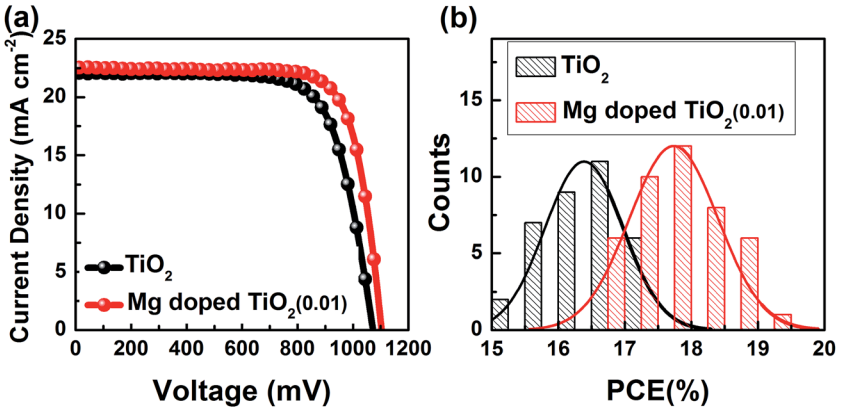

Fig. 3 (a) Illuminated I–V curves of the cells with different ETLs and (b) statistic histograms of their performance.

the cell does not change after ion doping since the ideality factors of the cells are almost the same.[28] This implies that no insulating layer is formed at the ETL/perovskite interface to accumulate free carriers,[36] which also confirms the above-mentioned discussion based on the XPS results.

The recombination properties are further investigated to understand the influence of Mg doping on the photoelectric characteristics of the cells. The saturated recombination current density (J_0) of the cell is derived from the I–V curves, as shown in Fig. 4(a).[28] It can be seen that J_0 is decreased from 3.15×10^{-7} to 1.97×10^{-7} mA cm^{-2} after Mg doping. In a heterojunction solar cell, J_0 is related to the built-in potential (V_{bi}) of the cell as $J_0 \sim \exp(-qV_{bi}/K_BT)$,[21,31] where q is the electron charge, K_B is the Boltzmann constant and T is the temperature. As the Fermi energy level of the ETL is shifted upward, it can be inferred that V_{bi} is also increased, thus decreasing J_0. According to the calculated J_0 and the ideality factor of the cell, V_{OC} can be estimated as $AK_BT/q \times \ln(J_{SC}/J_0)$.[28] With the value of J_0, it is found that V_{OC} is improved by about 30 mV, which agrees well with the experimental results. The AC impedance spectra are also applied to evaluate the charge recombination resistance (R_{CT}) and the accuracy of the abovementioned calculation based on the DC I–V results. Fig. 4(b) gives the Nyquist plots of the cells. After Mg doping, R_{CT} of the cell increases from 8 to about 13.5 kΩ cm^2, in good agreement with the theoretical relationship between R_{CT} and J_0.[37] Transient photovoltage in dark is also

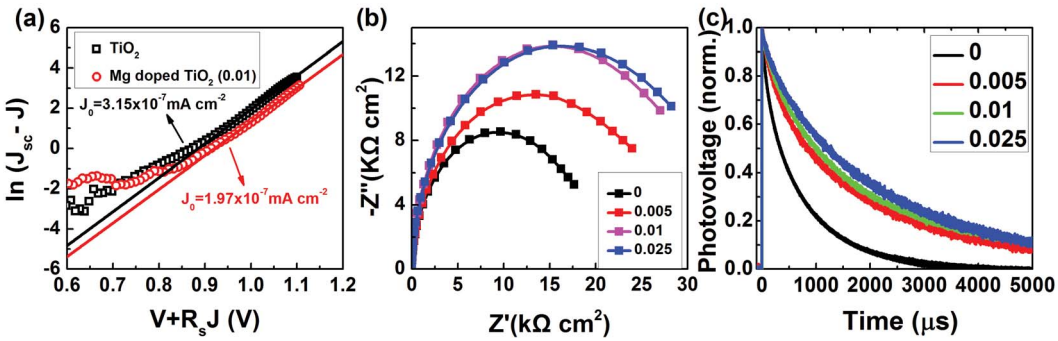

Fig. 4 (a) Plots of $\ln(J_{SC} - J)$ against $V + R_SJ$ derived from the illuminated I–V curves of the cell (Fig. 3(a)) and the linear fitting curves to get the saturated recombination current density (J_0). (b) Nyquist plots at 700 mV and (c) transient photovoltage results of the cells with different ETLs in dark.

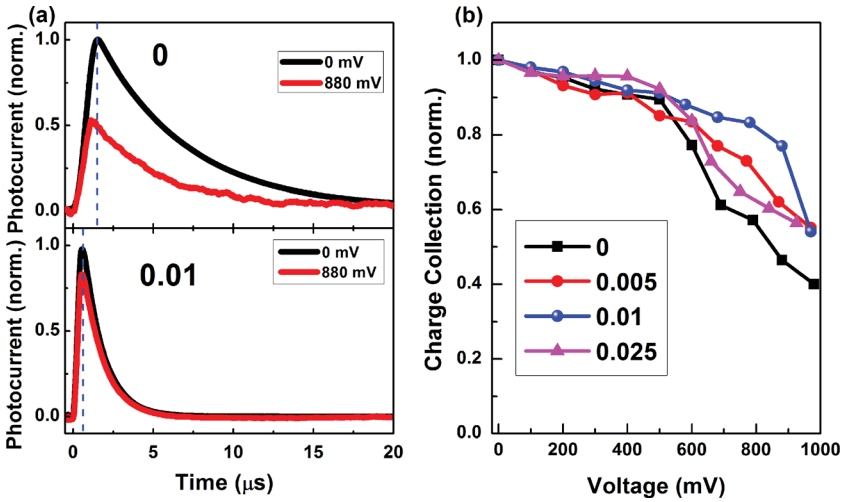

Fig. 5 (a) Transient photocurrent results of the cells with different ETLs under the illumination of 100 mW cm^{-2} and at bias voltages of 0 and 880 mV. (b) Normalized charge collection of the cells calculated with $\Delta Q/\Delta Q$ (0 mV), where ΔQ is the total collected photo-induced charge by integrating the transient photocurrents.

measured, as shown in Fig. 4(c). For the cell with the pristine TiO_2 ETL, it has a recombination lifetime of about 0.8 ms, which obviously increases to 1.7 ms after Mg doping. All these self-consistent results support that Mg doping can decrease the charge recombination in the cell, which agrees with the previous reports.[29] This can be reasonably explained by the change in the Fermi energy level.

In addition to the charge recombination, the increase in film conductivity may also influence the carrier transport ability of the cell and the final charge collection. Thus, the transient photocurrent of the cell at different bias voltages is measured for deep understanding.[30] Fig. 5(a) gives the transient photocurrent results of the cells with ETLs of the pristine TiO_2 and the Mg-doped TiO_2 (0.01), respectively, at bias voltages of 0 and 880 mV. For the cell without ETL doping, the carrier transport time (τ_j) is 5.5 μs at 0 mV. When the bias voltage is increased to 880 mV, wherein the solar cell may work in practice, the peak photocurrent decreases by about 50%. Moreover, the τ_j changes to 4.0 μs. The left shift of the photocurrent peak confirms this decrease.[38] By integrating the photocurrents, the total charge collected by the cell can be derived. As the energy of incident pulse laser does not change during the measurement, the results of transient photocurrent mean that the charge collection efficiency decreases by more than 50% when the bias voltage is increased. Another interesting result is the decrease in τ_j. In the general physics model of a heterojunction solar cell, the photo-induced free electrons in the perovskite absorber can be fast extracted into the ETL within several nanoseconds.[21] In this case, the non-equilibrium free electrons will stay close to the ETL/perovskite interface in a form of delta distribution. Furthermore, these carriers will spontaneously diffuse to the FTO/ETL interface to be collected. In this process, some carriers can also be recombined through the ETL/perovskite interface. These recombined carriers will not contribute to the photocurrent. The decrease in τ_j is usually thought to be attributed to the enhancement in charge conductivity.[38] However, in the planar perovskite solar cell, we find that the bias voltage would not change the electronic properties of the ETL by theoretical calculation and experimental measurements. Thus, it is supposed that the conductivity of the ETL does not enlarge by increasing the bias voltage. Moreover, the charge collection efficiency would not be significantly decreased if the conductivity is increased. Therefore, the only possibility is that more free carriers are recombined at the interface.[39] One may debate that the interface recombination during the carrier collection can be ignored since τ_j is much smaller than the generally measured and reported charge recombination lifetime. However, it can be noted that the recombination lifetime of the cell is found to be ultra-short under illumination and high bias voltages, which is only several microseconds, similar to τ_j. Thus, a high conductivity and short τ_j are necessary for high charge collection efficiency.

When it comes to the doped ETL, τ_j is only about 1.3 μs at bias voltage of 0 mV, whereas at 880 mV, τ_j is not changed. Moreover, the peak photocurrent only decreases by about 20%. All these results indicate that much fewer free carriers are lost during the transport and collection processes. The shorter τ_j and higher conductivity of the Mg doped ETL contributes to this positive effect. With the transient photocurrents, the total collected charge of different cells at different bias voltages is finally derived and summarized in Fig. 5(b). At low bias voltages below 500 mV, all the cells show almost the same charge collection efficiency. At higher voltages, the charge collection of the pristine TiO_2 ETL based cell decreases due to the increase in charge recombination. Although the charge recombination lifetime of the Mg doped ETL based cell can also significantly decrease at high voltages, the faster charge transport still prevents the obvious carrier loss and maintains higher charge collection efficiency. More efficient charge collection at high voltages could be the microscopic origin for the higher FF of the cell.

In particular, for the best performed device, the detailed *I–V* curve is shown in Fig. 6(a), giving a short-circuit current density

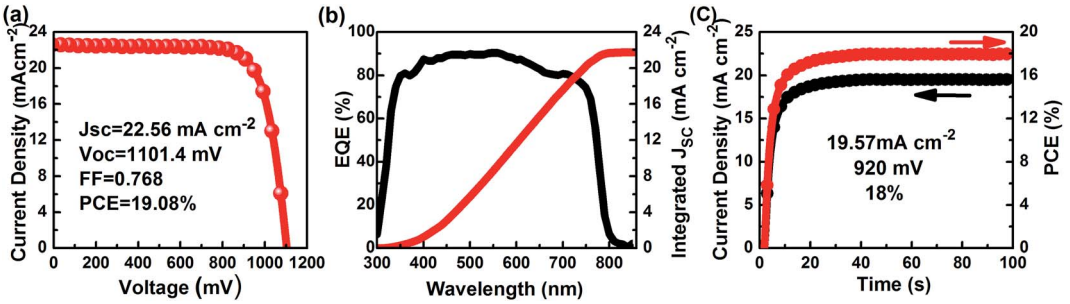

Fig. 6 (a) *I–V* curve with a scanning rate of 20 mV s^{-1}, (b) EQE spectrum and integrated J_{SC} and (c) steady-state current output and efficiency of the best performed cell with Mg doped ETL.

(J_{SC}) of 22.56 mA cm^{-2}, V_{OC} of 1101.4 mV, FF of 0.768, and PCE of 19.08%. The external quantum efficiency in the short-circuit condition is also measured, yielding an integrated J_{SC} of about 21.8 mA cm^{-2}, agreeing well with the *I–V* result and confirming the accuracy of our measurement. The steady-state current output and efficiency of the cell is also measured, as shown in Fig. 6(c). A steady-state PCE of 18% is obtained, which is only a little lower than the *I–V* result due to the anomalous hysteresis in this cell.

Conclusions

Mg has been introduced as an effective ion dopant to enhance the carrier transport ability of the compact TiO_2 ETL for planar perovskite solar cells. XPS valence band spectra reveal that this doping can shift the Fermi energy level of the ETL upward, increasing the free electron density or decreasing the density of deep trap states. With this doping, the resistivity of the TiO_2 film is decreased, leading to a decrease in the series resistance of the cell. Moreover, the cell performance is evidently boosted, yielding a PCE exceeding 19%. The microscopic carrier transport and recombination mechanisms behind the macroscopic efficiency are further investigated with DC current–voltage, AC frequency impedance and modulated transient photocurrent/photovoltage analysis. This doping can significantly reduce the transport time of photo-induced carriers to be collected, which obviously enhances the charge collection efficiency of the cell at high bias voltages. This improvement in charge collection efficiency contributes to higher FF and cell efficiency. In addition to improving the cell performance, the modulated electrical transient investigations applied in this work also give an effective approach to clarify the microscopic properties of a solar cell.

Acknowledgements

This study was supported by the Natural Science Foundation of China (Grant No. 51421002, 11474333, 91433205 and 51627803).

References

1 A. Kojima, K. Teshim, Y. Shirai and T. Miyasaka, *J. Am. Chem. Soc.*, 2009, **131**, 6050–6051.
2 H. S. Kim, C. R. Lee, J. H. Im, M. Grätzel and N. G. Park, *Sci. Rep.*, 2012, **2**, 591.
3 M. M. Lee, J. Teuscher, T. Miyasaka, T. N. Murakami and H. J. Snaith, *Science*, 2012, **338**, 643–647.
4 J. Burschka, N. Pellet, S. J. Moon, R. Humphry-Baker, P. Gao, M. K. Nazeeruddin and M. Grätzel, *Nature*, 2013, **499**, 316–319.
5 W. Li, J. Fan, J. Li, Y. Mai and L. Wang, *J. Am. Chem. Soc.*, 2015, **137**, 10399–10405.
6 S. Pang, Y. Zhou, Z. Wang, M. Yang, A. R. Krause, Z. Zhou, K. Zhu, N. P. Padture and G. Cui, *J. Am. Chem. Soc.*, 2016, **138**, 750–753.
7 NREL, http://www.nrel.gov/ncpv/images/efficiency_chart.jpg, accessed 2016.
8 M. Liu, M. B. Johnston and H. J. Snaith, *Nature*, 2013, **501**, 395–398.
9 X. Li, D. Bi, C. Yi, J. D. Décoppet, J. Luo, S. M. Zakeeruddin, A. Hagfeldt and M. Grätzel, *Sci. Adv.*, 2016, **353**, 58–62.
10 N. J. Jeon, J. H. Noh, W. S. Yang, Y. C. Kim, S. Ryu, J. Seo and S. I. Seok, *Nature*, 2014, **517**, 476–480.
11 W. S. Yang, J. H. Noh, N. J. Jeon, Y. C. Kim, S. Ryu, J. Seo and S. I. Seok, *Science*, 2015, **348**, 1234–1237.
12 M. Xiao, F. Huang, W. Huang, Y. Dkhissi, Y. Zhu, J. Etheridge, A. Gray-Weale, U. Bach, Y. B. Cheng and L. Spiccia, *Angew. Chem., Int. Ed.*, 2014, **53**, 1–7.
13 Z. Xiao, Q. Dong, C. Bi, Y. Shao, Y. Yuan and J. Huang, *Adv. Mater.*, 2014, **26**, 6503–6509.
14 Z. Xiao, C. Bi, Y. Shao, Q. Dong, Q. Wang, Y. Yuan, C. Wang, Y. Gao and J. Huang, *Energy Environ. Sci.*, 2014, **7**, 2619–2623.
15 H. Zhang, J. Shi, J. Dong, X. Xu, Y. Luo, D. Li and Q. Meng, *J. Energy Chem.*, 2015, **24**, 707–711.
16 J. P. C. Baen, L. Steier, W. Tress, M. Saliba, S. Neutzner, T. Matsui, M. Grätzel and A. Hagfeldt, *Energy Environ. Sci.*, 2015, **8**, 2928–2934.
17 H. Ting, L. Ni, S. Ma, Y. Ma, L. Xiao and Z. Chen, *Acta Phys. Sin.*, 2015, **64**, 038802.
18 H. Zhou, Q. Chen, G. Li, S. Luo, T. Song, H. Duan, Z. Hong, J. You, Y. Liu and Y. Yang, *Science*, 2014, **345**, 542–546.
19 X. Yang, H. Chen, E. Bi and L. Han, *Acta Phys. Sin.*, 2015, **64**, 038404.
20 L. Zhu, J. Shi, D. Li and Q. Meng, *Acta Chim. Sin.*, 2015, **73**, 261–266.
21 J. Shi, X. Xu, D. Li and Q. Meng, *Small*, 2015, **11**, 2472–2486.

22 J. T. W. Wang, J. M. Ball, E. M. Barea, A. Abate, J. A. Alexander-Webber, J. Huang, M. Saliba, I. Mora-Sero, J. Bisquert, H. J. Snaith and R. J. Nicholas, *Nano Lett.*, 2014, **14**, 724–730.
23 Z. Zhu, J. Ma, Z. Wang, C. Mu, Z. Fan, L. Du, Y. Bai, L. Fan, H. Yan, D. L. Phillips and S. Yang, *J. Am. Chem. Soc.*, 2014, **136**, 3760–3763.
24 B. Chen, H. Rao, W. Li, Y. Xu, H. Chen, D. Kuang and C. Su, *J. Mater. Chem. A*, 2016, **4**, 5647–5653.
25 X. Yin, Y. Guo, Z. Xue, P. Xu, M. He and B. Liu, *Nano Res.*, 2015, **8**, 1997–2003.
26 F. Giordano, A. Abate, J. P. C. Baena, M. Saliba, T. Matsui, S. H. Im, S. M. Zakeeruddin, M. K. Nazeeruddin, A. Hagfeldt and M. Graetzel, *Nat. Commun.*, 2015, **7**, 10379.
27 J. H. Heo, M. S. You, M. H. Chang, W. Yin, T. K. Ahn, S. J. Lee, S. J. Sung, D. H. Kim and S. H. Im, *Nano Energy*, 2015, **15**, 530–539.
28 J. Shi, J. Dong, S. Lv, Y. Xu, L. Zhu, J. Xiao, X. Xu, H. Wu, D. Li, Y. Luo and Q. Meng, *Appl. Phys. Lett.*, 2014, **104**, 063901.
29 J. Wang, M. Qin, H. Tao, W. Ke, Z. Chen, J. Wan, P. Qin, L. Xiong, H. Lei, H. Yu and G. Fang, *Appl. Phys. Lett.*, 2015, **106**, 121104.
30 J. Shi, X. Xu, H. Zhang, Y. Luo, D. Li and Q. Meng, *Appl. Phys. Lett.*, 2015, **107**, 163901.
31 S. M. Sze and K. K. Ng, *Physics of Semiconductor Devices*, Wiley, New York, 3rd edn, 2006.
32 Y. Wu, X. Yang, H. Chen, K. Zhang, C. Qin, J. Liu, W. Peng, A. Islam, E. Bi, F. Ye, M. Yin, P. Zhang and L. Han, *Appl. Phys. Express*, 2014, **7**, 5.
33 K. Wojciechowski, M. Saliba, T. Leijtens, A. Abate and H. J. Snaith, *Energy Environ. Sci.*, 2014, **7**, 1142–1147.
34 X. Guo, Y. Luo, C. Li, D. Qin, D. Li and Q. Meng, *Curr. Appl. Phys.*, 2012, **12**, 54–58.
35 X. Guo, Y. Luo, Y. Zhang, X. Huang, D. Li and Q. Meng, *Rev. Sci. Instrum.*, 2010, **81**, 103106.
36 H. Wei, J. Shi, X. Xu, J. Xiao, J. Luo, J. Dong, S. Lv, L. Zhu, H. Wu, D. Li, Y. Luo, Q. Meng and Q. Chen, *Phys. Chem. Chem. Phys.*, 2015, **17**, 4937–4944.
37 J. Shi, Y. Luo, H. Wei, J. Luo, J. Dong, S. Lv, J. Xiao, Y. Xu, L. Zhu, X. Xu, H. Wu, D. Li and Q. Meng, *ACS Appl. Mater. Interfaces*, 2014, **6**, 9711–9718.
38 P. R. F. Barnes, K. Miettunen, X. Li, A. Y. Anderson, T. Bessho, M. Gratzel and B. C. O'Regan, *Adv. Mater.*, 2013, **25**, 1881–1922.
39 D. S. Shen and S. Wagner, *J. Appl. Phys.*, 1996, **79**, 794.
40 X. Xia, H. Li, Y. Li, C. Liu and X. Liu, *J. Energy Chem.*, 2015, **24**, 693–697.
41 Q. Xue, C. Sun, Z. Hu, F. Huang, H. L. Yip and Y. Cao, *Acta Chim. Sin.*, 2015, **73**, 179–192.
42 X. Xu, H. Zhang, J. Shi, J. Dong, Y. Luo, D. Li and Q. Meng, *J. Mater. Chem. A*, 2015, **3**, 19288–19293.
43 H. Kim, K. G. Lim and T. W. Lee, *Energy Environ. Sci.*, 2015, **9**, 12–30.
44 J. Dong, J. Shi, D. Li, Y. Luo and Q. Meng, *Appl. Phys. Lett.*, 2015, **107**, 073507.